Title

Layered Hybrid Lead Iodide Perovskites with Short Interlayer Distances

Authors

Mao, Lingling
Morgan, Emily E
Li, Alice
et al.

Publication Date

2022-08-02

DOI

10.1021/acsenergylett.2c01321

Peer reviewed

Layered Hybrid Lead Iodide Perovskites with Short Interlayer Distances

Lingling Mao[1*], Emily E. Morgan[2], Alice Li[2], Rhiannon M. Kennard[2], Min Ji Hong[3], Yang Liu[1], Clayton J. Dahlman[2], John G. Labram[3,4], Michael L. Chabinyc[2] and Ram Seshadri[2*]

[1]Department of Chemistry, Southern University of Science and Technology, Shenzhen, Guangdong 518055, China
[2]Materials Research Laboratory and Materials Department, University of California, Santa Barbara, California 93106, United States
[3]School of Electrical Engineering and Computer Science, Oregon State University, Corvallis, OR 97331, United States
[4]Department of Electronic & Electrical Engineering, University College London, London WC1E 7JE, United Kingdom

*Email addresses: maoll@sustech.edu.cn and seshadri@mrl.ucsb.edu

ABSTRACT: Layered hybrid perovskites comprise modular components that are individually highly tunable, resulting in materials with a range of structure and properties. In these layered materials, the usual assumption is of two-dimensional electronic behavior, because of the relatively large separations between the inorganic layers. Here, we report two layered hybrid lead iodide perovskites that possess unusually short interlayer distances: $(IPA)_2(MA)Pb_2I_7$ and $(ACA)(MA)PbI_4$ (IPA = iso-propylammonium, MA = methylammonium, ACA = acetamidinium). These compounds are prepared from mixing small organic cations, where they crystallize in the Ruddlesden-Popper type structure, and a structure with alternating cations in the interlayer space, respectively. The crystal structures are compared in detail with related structures, and electronic structures are analyzed using density-functional theory-based calculations. Time-resolved microwave conductivity measurements are employed to provide insight into charge transport in these compounds. This work exemplifies the unusual templating role of small organic cations in the layered halide compounds.

Hybrid layered halide perovskites are attractive semiconductors due to their highly tunable properties.[1,2] Establishing structure-property relations associated with optoelectronic performance has resulted in a number of high-performance photovoltaics in this family of materials.[3-7] As research in this field has advanced, several different structure-types have been identified and classified, similar to oxide perovskites, where the two main categories are the Ruddlesden-Popper (RP) and Dion-Jacobson (DJ).[8,9] The general formula for the 2D structures is $A'_mA_{n-1}M_nX_{3n+1}$, where m = 2 for RP phases and m = 1for DJ phases.[2] The preference to form either an RP or DJ phase arises from differences in the charge and functional group of the organic spacing cations.[2] These differences result in subtle changes of the inorganic framework, and subsequently the optical properties.[2,10]

An interesting open question in the 2D halide perovskite world is how close the inorganic layers can be without linking together through chemical bonds, as in the 3D perovskite. For example, one can imagine filling increasingly small organic/inorganic cations between the inorganic sheets, while simultaneously maintaining the corner-sharing octahedra layer ordering. The closest distance possible should arise from the use of the smallest cations, such as Cs, methylammonium (MA) or formamidinium (FA). For instance, the mixed-halide all-inorganic 2D perovskites $Cs_2PbCl_2I_2$ and $Cs_2SnCl_2I_2$ have interlayer distances of ~3.1 Å,[11,12] one of the closest interlayer distances reported to-date. $(MA)_2Pb(SCN)_2I_2$ also has a very close interlayer distance, and lower energy band gap compared with conventional 2D halide perovskites.[13,14] In another recently reported layered material $(MHy)_2PbI_4$ (MHy = methylhydrazinium),[15] the methylhydrazinium cation fits in the 3D distorted perovskite cages for the Cl- and Br-based structure,[16] but only forms the 2D structure in the case of the iodide. This material has even smaller interlayer distance of ~3.0 Å for the unique cation orientation, and a low energy gap of 2.20 eV.[15] Mixing small cations such as MA, Cs and guanidinium (GA) results in a distinct type of 2D perovskite, namely the alternating cation in the interlayer space (ACI) type,[17-19] where the n = 1 to 3 has been reported with reduced energy gaps compared with similar RP phases.[18]

The feature of short interlayer distances in 2D halide perovskite has significant implications for their optoelectronic properties, related to the quantum and dielectric confinement in these layered materials.[20,21] Light illumination on DJ, ACI and RP phases, results in short-interlayered phases (DJ and ACI) showing a contraction of the 2D layers in comparison to the RP phases, which remain almost unchanged.[6] This effect boosts the corresponding performance of the DJ- and ACI-based solar cells. The transient photoluminescence mapping on DJ phase $(4AMP)(MA)Pb_2I_7$, has revealed that the transport of carriers or excitons along the out-of-plane direction is comparable to along the in-plane direction.[22] This is dramatically different from the RP phase, where the carrier transport along the in-plane direction is usually superior to that of the out-of-plane direction because of the long interlayer distances.

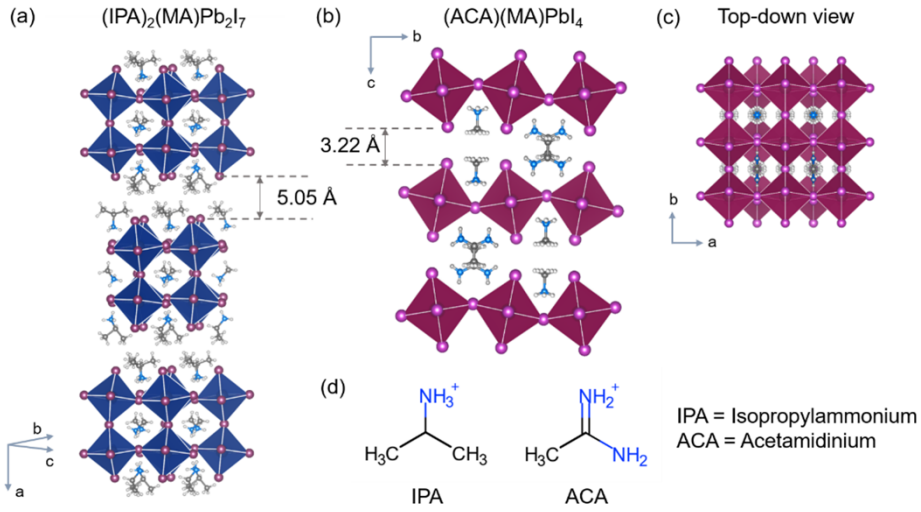

Figure 1. (a) Crystal structure of $(IPA)_2(MA)Pb_2I_7$. (b) Crystal structure of $(ACA)(MA)PbI_4$ viewed parallel to the *a* axis and (c) parallel to the *c* axis. (d) Structure of the spacing cations used in this work. Blue and fuchsia octahedron denote $[PbI_6]$. IPA = iso-propylammonium, MA = methylammonium, ACA = acetamidinium.

Here, we report prototype phases of hybrid 2D halide perovskite with short interlayer distances by incorporating selected small organic cations. These compounds can be difficult to access synthetically because of the risk of producing mixed phases from mixing small cations. However, we find that a judicious mix of methylammonium (MA) and iso-propylammonium (IPA) with PbO in HI results in the formation of a bilayer (n = 2) RP type 2D perovskite structure $(IPA)_2(MA)Pb_2I_7$. Additionally, we find that a mix of MA and acetamidinium (ACA) forms an ACI-type structure with the composition $(ACA)(MA)PbI_4$. Notably, both small cations (IPA and ACA) would not form layered structures with lead iodide by themselves. Instead, IPA forms corner-sharing 1D zig-zag chains $(IPA)_3Pb_2I_5$ in hydriodic acid with PbO. This structure has been previously reported and we also collected the crystal structure for reference [see Figure S1(a)]. Similarly, ACA (acetamidinium) forms another type of more commonly seen type of structure $(ACA)PbI_3$, where $[PbI_6]$ octahedra are linked in a face-sharing manner [Figure S1(b)]. With the addition of MA and proper ratio of the starting materials, two new layered structures $(IPA)_2(MA)Pb_2I_7$ and $(ACA)(MA)PbI_4$ form. The detailed experimental procedure is recorded in the Methods section.

$(IPA)_2(MA)Pb_2I_7$ crystalizes in the tetragonal space group $P4_2/mnm$, as seen in Figure 1a (data presented in Table S1). This structure belongs to the RP family $(A'_2A_{n-1}M_nX_{3n+1})$ with n = 2, and the A' spacing cation IPA is likely the smallest spacing cation reported, with a fairly short interlayer distance of 5.05 Å. Considering the Pb-I bond distance is ~3.0 Å, the interlayer distance here is similar to the size of the perovskite cage (*i.e.* 2×Pb-I bond). Interestingly, IPA forms a two-layered RP structure $(IPA)_3Sn_2I_7$ with tin iodide at high temperatures, but this phase converts to $(IPA)_3SnI_5$ at room temperature. Both structures have been reported previously.[23]

In contrast, $(ACA)(MA)PbI_4$, belongs to a different structural type, the alternating cation in the interlayer space (ACI) type [Figure 1(b-c)] (data presented in Table S2). The crystal structure is analogous to $(GA)(MA)PbI_4$[18] and $(Tu)(MA)PbI_4$[24] (Tu = protonated thiourea), and it crystallizes in the same orthorhombic space group *Imma*. In fact, these three structures are almost identical, due to the fact that ACA, GA and Tu are similar in size and shape. The only structural difference aside from the cation used is a small difference the Pb-I-Pb angles. The chemical structures of IPA and ACA are both shown in Figure 1(d), and the resemblance is clear. We therefore believe that the conjugation present in the ACA cation is critical in the formation of ACI-type phases, as GA is also a conjugated cation, which is a consequence of conjugation holding all of the C and N atoms on the same plane.[18] Both compounds could be prepared as phase-pure powders as shown in Figure S2.

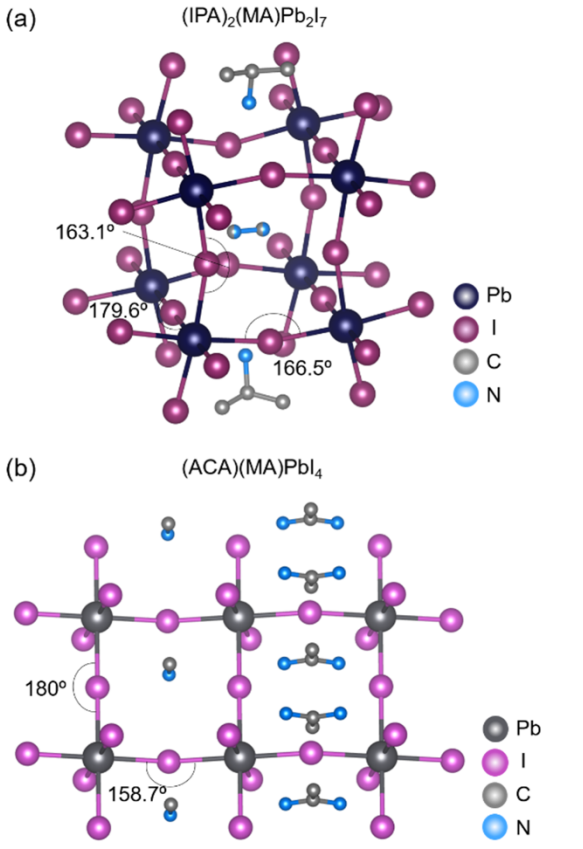

Figure 2. Detailed view of Pb-I-Pb angles in (a) $(IPA)_2(MA)Pb_2I_7$ and (b) $(ACA)(MA)PbI_4$. Hydrogens are omitted for clarity.

Because of the nature of the small primary ammonium IPA cation, the inorganic Pb-I framework undergoes a similar level of distortion compared with the more studied $(BA)_2(MA)Pb_2I_7$. Significant distortion arises when the cation is too small, too large, or in the presence of other interactions (*i.e.* H-bonding). In this particular case, IPA is too small to stabilize the space of the interlayer, causing a "relaxation" of the inorganic framework, which manifests as distortion. The horizontal and vertical Pb-I-Pb angles are 166.5°, 179.6°, and 163.1°, respectively (Figure 2a). In the case of $(ACA)(MA)PbI_4$, the structure has a unique cation arrangement (see Figure 2b), where MA and ACA occupy alternating sites of the interlayer space. The ACA cations are packed in an alternating array, with the regular ones staying in the middle of the layer and the irregular ones are on top of the iodides. As stated previously, the structures of $(ACA)(MA)PbI_4$ and $(GA)(MA)PbI_4$ are almost identical, where $(GA)(MA)PbI_4$ has Pb-I-Pb angles of 180.0° and 159.0°, $(ACA)(MA)PbI_4$ has Pb-I-Pb angles of 180.0° and 158.7° [Figure 2(b)].

At this point, it is necessary to discuss the effect of cation arrangement on optical properties for the n = 1 structures. For the 1+ organic cations, we can divide them into three types as seen in Figure 3(a). Type I is the most commonly-seen RP-type, where the protonated ammonium group points towards the inorganic layer and the tails are oriented towards the interlayer

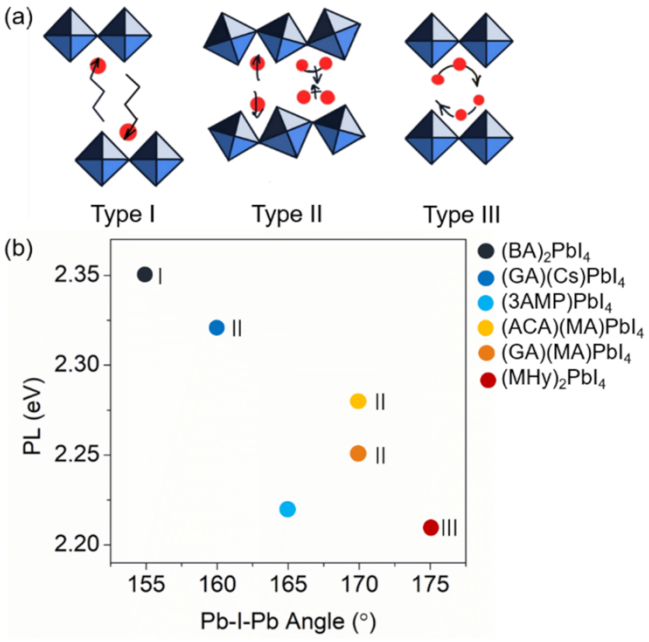

Figure 3. (a) Illustration of cation orientations in 2D halide perovskites as discussed in the text. (b) Correlation between averaged Pb-I-Pb angle and PL emission energy in a representative group of type I, II and III structure. PL emission energies for $(3AMP)PbI_4$, $(MHy)_2PbI_4$, $(GA)(Cs)PbI_4$, and $(GA)(MA)PbI_4$ are from ref. 9, 15, 17, 18, respectively.

space. Type II is the ACI type, which differentiates itself with two different ordered cations in the interlayer space in one structure. Type III is also very interesting in the sense that it requires a small organic cation to orient in an unusual tilted configuration which maximizes hydrogen bonding in the structure (Figure 3a). This type is known for the example of $(MHy)_2PbI_4$ (MHy = methylhydrazinium), which exhibits the lowest energy

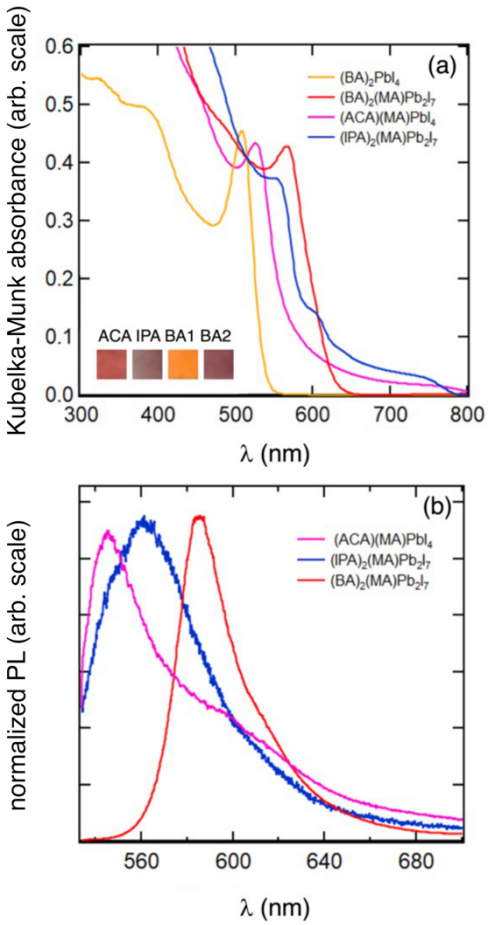

Figure 4. (a) Optical absorption spectra of $(IPA)_2(MA)Pb_2I_7$ and $(ACA)(MA)PbI_4$. $(BA)_2PbI_4$ and $(BA)_2(MA)Pb_2I_7$ are presented for comparison. Inset shows picture of powdered samples of the compounds measured here. (b) PL emission spectra of $(IPA)_2(MA)Pb_2I_7$, $(ACA)(MA)PbI_4$, and $(BA)_2(MA)Pb_2I_7$.

of PL emission amongst all comparable structures (Figure 3b). The average Pb-I-Pb angle is 175°, close to the perfect 180°. The ACI types (type II) are in the middle, where $(ACA)(MA)PbI_4$ and $(GA)(MA)PbI_4$ have lower PL emission energy and $(GA)CsPbI_4$ has higher PL emission energy, due to the smaller average Pb-I-Pb angles. This is because Cs is a smaller cation than MA, and it therefore has less ability to stabilize the Pb-I framework, causing a contraction of the layer and smaller average angles. Type I, represented by classic RP phase $(BA)_2PbI_4$, has the highest PL emission energy and the smallest Pb-I-Pb angles. Note that $(3AMP)PbI_4$ (3AMP = 3-aminomethylpiperidinium) is a DJ phase which does not belong to any of the three types.[9] Though the averaged bond angles are not as large, the use of the 3AMP di-cation leads to the direct alignment of the layers (as opposed to the staggered configuration seen in RP phases) and a short interlayer distance of ~4 Å. The stronger iodine-iodine interaction arising from the direct alignment and short interlayer distance is potentially influential in lowering the band gap and PL emission. The analysis of the structure-PL relations is fundamentally important to the design and synthesis of new layered perovskite materials.

The optical properties of the short-interlayer-distance phases are characterized at room temperature. The absorption edges of $(ACA)(MA)PbI_4$ and $(IPA)_2(MA)Pb_2I_7$ are at 2.17 and 2.10 eV (Figure 4a), respectively. We have measured the absorption spectra of $(BA)_2PbI_4$ and $(BA)_2(MA)Pb_2I_7$ for comparison, and

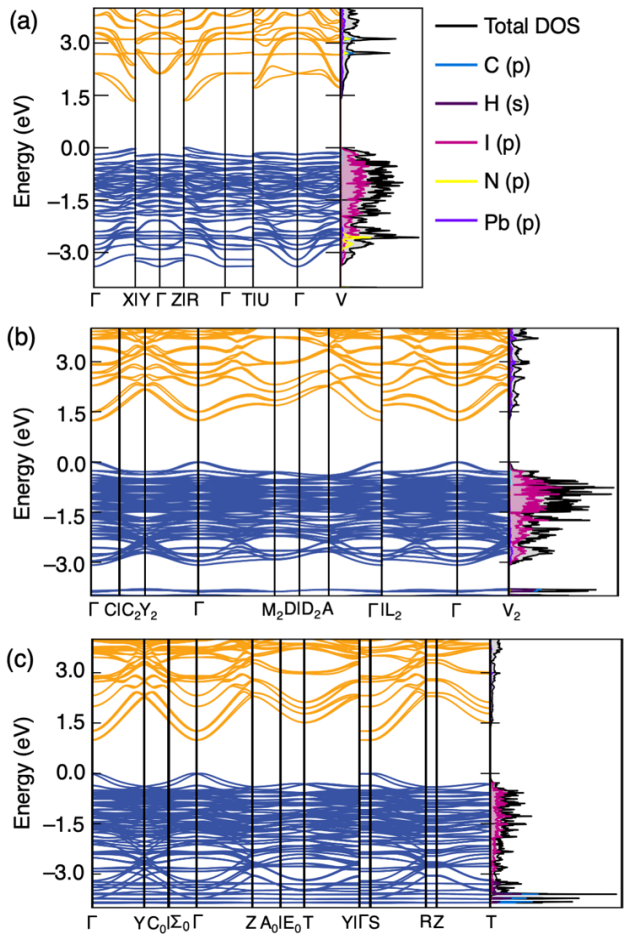

Figure 5. Density of states and band structure for (a) (ACA)(MA)PbI_4, (b) $(IPA)_2(MA)Pb_2I_7$, and (c) $(BA)_2(MA)Pb_2I_7$.

(ACA)(MA)PbI_4 and $(IPA)_2(MA)Pb_2I_7$ clearly fall in between these two. The colors of the polycrystalline powder samples provide further evidence of the band gap trend (Figure 4a, inserted), where $(BA)_2PbI_4$ is orange, (ACA)(MA)PbI_4 is red, $(IPA)_2(MA)Pb_2I_7$ and $(BA)_2(MA)Pb_2I_7$ are dark red. For $(IPA)_2(MA)Pb_2I_7$, there is a slight bump at ~620 nm (2 eV). We later recollected the absorbance spectrum from a different batch of samples (see Figure S3), and found the band edge should be around ~590 nm (2.10 eV). We then collected the PL emission spectra [Figure 4(b)] using a confocal Raman instrument with a 532 nm laser excitation. This instrument was chosen partially due to the rather weak PL observed compared with other compounds such as $(BA)_2(MA)Pb_2I_7$, as evidenced by the roughness of the normalized PL spectra in Figure 4(b). We believe that the fast precipitation process during synthesis results in poor crystallinity of (ACA)(MA)PbI_4 and $(IPA)_2(MA)Pb_2I_7$, leading to overall weaker PL. Additionally, the PL of $(BA)_2PbI_4$ is not plotted here because of the 532 nm excitation cut-off. The PL emission energy follows the same trend as the absorption edge, where (ACA)(MA)PbI_4 > $(IPA)_2(MA)Pb_2I_7$ > $(BA)_2(MA)Pb_2I_7$. The shape of the PL emission spectra of (ACA)(MA)PbI_4 and $(IPA)_2(MA)Pb_2I_7$ are also unusually broad compared to similar compounds.

In order to further investigate the electronic structure of these new phases, we performed density functional theory (DFT) calculations using the PBE functional and incorporating spin-orbit coupling to determine the band structure and density of states for (ACA)(MA)PbI_4 and $(IPA)_2(MA)Pb_2I_7$, and compared the results with $(BA)_2(MA)Pb_2I_7$ (Figure 5). The trend in the calculated band gaps qualitatively match the experimental trends, with a calculated gap of 1.34 eV for (ACA)(MA)PbI_4, 1.24 eV for $(IPA)_2(MA)Pb_2I_7$, and 1.00 eV for $(BA)_2(MA)Pb_2I_7$. In the case of all compounds the bandgap is underestimated due to the use of the PBE functional with the spin-orbit coupling correction. Additionally, calculations indicate that all compounds are direct-gap semiconductors. For (ACA)(MA)PbI_4, the direct gap occurs at the R point, and for $(IPA)_2(MA)Pb_2I_7$ and $(BA)_2(MA)Pb_2I_7$, the direct gap occurs at Γ. In all three compounds, the valence band maximum is comprised mainly of iodine 5p states, while the conduction band minimum is made up of lead 6p states. As would be expected from the crystal structures of these compounds, the band structures of $(IPA)_2(MA)Pb_2I_7$ and $(BA)_2(MA)Pb_2I_7$ are qualitatively similar and show similar degrees of band dispersion in the valence band and conduction band. These observations are also consistent with literature reports of the band structure of related RP compounds. In contrast, in (ACA)(MA)PbI_4 the conduction bands are dispersed while the valence bands are fairly flat. This can partially be attributed to the fact that (ACA)(MA)PbI_4 is an n = 1 structure, while both $(IPA)_2(MA)Pb_2I_7$ and $(BA)_2(MA)Pb_2I_7$ are n = 2. Additionally, this suggests that although there may be some 3D-character to this structure (as indicated by the small amount of dispersion in the valence band maximum along Γ to Z), it is likely weak. The rather flat bands also corroborated by the results of the TRMC measurements, discussed below. A notable additional feature of the electronic structure of (ACA)(MA)PbI_4 is the more obvious contribution of the organic cation to the DOS in the energy range shown. These features have also been observed for similar compounds and are due to the conjugation of the ACA cation.[17] Overall, although $(IPA)_2(MA)Pb_2I_7$ displays a small interlayer spacing, its electronic structure is quite similar to other n = 2 RP phases. Additionally, (ACA)(MA)PbI_4 shows features seen in other ACI compounds, and the lack of dispersion in the band edges suggests that carrier mobility is unlikely to be high in this compound despite the reduced interlayer spacing.

Thin films were fabricated and characterized (Figure S4 to S7) of these two phases for time-resolved microwave conductivity (TRMC) measurements. TRMC is a contactless technique which enables one to approximate a proxy for carrier mobility and lifetime in thin-film semiconductors.[24] The common TRMC figure of merit is $\phi\Sigma\mu = \phi(\mu_e + \mu_h)$, where ϕ is the carrier generation yield (between 0 and 1), and μ_e and μ_h are the average mobility of electrons and holes, respectively, over the sample area. While $\phi\Sigma\mu$ has the same units as mobility, it contains contributions from both electrons and holes, and is also reduced by ϕ. In 3D perovskites, such as (MA)PbI_3, the exciton binding energy is known to be less than thermal energy at room temperature,[25] and ϕ is hence assumed to be close to unity. Under these circumstances $\phi\Sigma\mu$ can be interpreted in a similar way to mobility. However, in more excitonic systems such as organic semiconductors[26] or layered hybrid halides[27] this may not be the case.

Towards that goal, a thin film of (ACA)(MA)PbI_4 has been successfully made. A thin film of target composition $(IPA)_2(MA)Pb_2I_7$ yielded the n = 2 phase in bulk, but inclusions of higher n RP phases were identified via PL, and TRMC experiments are not reported in this compound. TRMC data for

thin-film samples of $(ACA)(MA)PbI_4$, $(BA)_2PbI_4$ and $(MA)PbI_3$ are presented in the supporting information, section S4, with the raw TRMC data displayed in Figure S8 and S9. Figure S10 to S12 display the processing of the TRMC data. Preliminary results (Table S3) indicate $\phi\Sigma\mu$ for $(ACA)(MA)PbI_4$ ($\phi\Sigma\mu = 0.014$ cm^2/Vs) is lower than for $(BA)_2PbI_4$ ($\phi\Sigma\mu = 0.076$ cm^2/Vs). Both 2D samples are one order of magnitude lower than the 3D film sample $(MA)PbI_3$ ($\phi\Sigma\mu = 0.66$ cm^2/Vs), for which the measured value is consistent with previous reports.[28] This is not unexpected as the average connectivity, and hence mobility, in a random direction is anticipated to be higher in a 3D system than a 2D system. Additionally, while the role-played by excitons is unclear in these compounds, it likely that ϕ will be higher in a 3D system than a 2D system.

To summarize, we report here two new short-interlayer-distanced 2D lead iodide perovskites $(IPA)_2(MA)Pb_2I_7$ and $(ACA)(MA)PbI_4$ and study their optical and electronic properties. A shared structural feature of these two new materials is the rather short interlayer distance (3 to 5 Å). These two materials have similar bandgaps of ≈2 eV and room-temperature observable PL. The short interlayer distance and small distortion in the inorganic framework give rise to a lower energy PL emission for $(ACA)(MA)PbI_4$, comparing with some other n = 1 structures, whereas $(IPA)_2(MA)Pb_2I_7$ has weaker and broader PL emission compared with $(BA)_2(MA)Pb_2I_7$. The electronic calculation reveal that the short interlayer distance does not necessarily bring large band dispersion. On the contrary, the rather flat bands correlate with low TRMC and PL intensity. Another possible reason for the low intensities could be from the structural instability, as the blend of these cations can lead to multiple phases. This work represents one step further in fine-tuning the structural nuances for the 2D halide perovskite family and provides more insights towards their application in high-performance optoelectronics.

ASSOCIATED CONTENT

The Supporting Information is available free of charge at https://pubs.acs.org/doi/10.1021/xxxxxx. Experimental details, structure of other related phases, additional thin-film data and preliminary TRMC data (PDF). Crystallographic cif. files for $(IPA)_2(MA)Pb_2I_7$ (CIF) and $(ACA)(MA)PbI_4$ (CIF).

AUTHOR INFORMATION

*Corresponding Author

maoll@sustech.edu.cn and seshadri@mrl.ucsb.edu

ACKNOWLEDGMENT

This work was supported by the Department of Energy, Office of Science, Basic Energy Sciences, under Grant SC0012541. The research reported here made use of the shared facilities of the Materials Research Science and Engineering Center at UC Santa Barbara, NSF DMR 1720256. The UCSB MRSEC is a member of the Materials Research Facilities Network (www.mrfn.org). We additionally acknowledge support from the Center for Scientific Computing at UCSB, supported by the NSF CNS-1725797 and NSF DMR-1720256. M.J.H. and J.G.L acknowledge the National Science Foundation for financial support (award number: 1942558). We are grateful to Professor Haipeng Lu for help with characterization.

REFERENCES

(1) Saparov, B.; Mitzi, D. B. Organic–Inorganic Perovskites: Structural Versatility for Functional Materials Design. *Chem. Rev.* **2016**, *116*, 4558-4596.

(2) Mao, L.; Stoumpos, C. C.; Kanatzidis, M. G. Two-Dimensional Hybrid Halide Perovskites: Principles and Promises. *J. Am. Chem. Soc.* **2019**, *141*, 1171-1190.

(3) Tsai, H.; Nie, W.; Blancon, J.-C.; Stoumpos, C. C.; Asadpour, R.; Harutyunyan, B.; Neukirch, A. J.; Verduzco, R.; Crochet, J. J.; Tretiak, S.; Pedesseau, L.; Even, J.; Alam, M. A.; Gupta, G.; Lou, J.; Ajayan, P. M.; Bedzyk, M. J.; Kanatzidis, M. G.; Mohite, A. D. High-efficiency two-dimensional Ruddlesden–Popper perovskite solar cells. *Nature* **2016**, *536*, 312-316.

(4) Liang, C.; Gu, H.; Xia, Y.; Wang, Z.; Liu, X.; Xia, J.; Zuo, S.; Hu, Y.; Gao, X.; Hui, W.; Chao, L.; Niu, T.; Fang, M.; Lu, H.; Dong, H.; Yu, H.; Chen, S.; Ran, X.; Song, L.; Li, B.; Zhang, J.; Peng, Y.; Shao, G.; Wang, J.; Chen, Y.; Xing, G.; Huang, W. Two-dimensional Ruddlesden–Popper layered perovskite solar cells based on phase-pure thin films. *Nat. Energy* **2021**, *6*, 38-45.

(5) Zhang, F.; Park, S. Y.; Yao, C.; Lu, H.; Dunfield, S. P.; Xiao, C.; Uličná, S.; Zhao, X.; Hill, L. D.; Chen, X.; Wang, X.; Mundt, L. E.; Stone, K. H.; Schelhas, L. T.; Teeter, G.; Parkin, S.; Ratcliff, E. L.; Loo, Y.-L.; Berry, J. J.; Beard, M. C.; Yan, Y.; Larson, B. W.; Zhu, K. Metastable Dion-Jacobson 2D structure enables efficient and stable perovskite solar cells. *Science* **2022**, *375*, 71-76.

(6) Li, W.; Sidhik, S.; Traore, B.; Asadpour, R.; Hou, J.; Zhang, H.; Fehr, A.; Essman, J.; Wang, Y.; Hoffman, J. M.; Spanopoulos, I.; Crochet, J. J.; Tsai, E.; Strzalka, J.; Katan, C.; Alam, M. A.; Kanatzidis, M. G.; Even, J.; Blancon, J.-C.; Mohite, A. D. Light-activated interlayer contraction in two-dimensional perovskites for high-efficiency solar cells. *Nat. Nanotechnol.* **2022**, *17*, 45-52.

(7) Mitzi, D. B.; Feild, C. A.; Harrison, W. T. A.; Guloy, A. M. Conducting tin halides with a layered organic-based perovskite structure. *Nature* **1994**, *369*, 467-469.

(8) Stoumpos, C. C.; Cao, D. H.; Clark, D. J.; Young, J.; Rondinelli, J. M.; Jang, J. I.; Hupp, J. T.; Kanatzidis, M. G. Ruddlesden–Popper Hybrid Lead Iodide Perovskite 2D Homologous Semiconductors. *Chem. Mater.* **2016**, *28*, 2852-2867.

(9) Mao, L.; Ke, W.; Pedesseau, L.; Wu, Y.; Katan, C.; Even, J.; Wasielewski, M. R.; Stoumpos, C. C.; Kanatzidis, M. G. Hybrid Dion–Jacobson 2D Lead Iodide Perovskites. *J. Am. Chem. Soc.* **2018**, *140*, 3775-3783.

(10) Li, X.; Hoffman, J. M.; Kanatzidis, M. G. The 2D Halide Perovskite Rulebook: How the Spacer Influences Everything from the Structure to Optoelectronic Device Efficiency. *Chem. Rev.* **2021**, *121*, 2230-2291.

(11) Li, J.; Yu, Q.; He, Y.; Stoumpos, C. C.; Niu, G.; Trimarchi, G. G.; Guo, H.; Dong, G.; Wang, D.; Wang, L.; Kanatzidis, M. G. $Cs_2PbI_2Cl_2$, All-Inorganic Two-Dimensional Ruddlesden–Popper Mixed Halide Perovskite with Optoelectronic Response. *J. Am. Chem. Soc.* **2018**, *140*, 11085-11090.

(12) Li, J.; Stoumpos, C. C.; Trimarchi, G. G.; Chung, I.; Mao, L.; Chen, M.; Wasielewski, M. R.; Wang, L.; Kanatzidis, M. G. Air-Stable Direct Bandgap Perovskite Semiconductors: All-Inorganic Tin-Based Heteroleptic Halides $A_xSnCl_yI_z$ (A = Cs, Rb). *Chem. Mater.* **2018**, *30*, 4847-4856.

(13) Daub, M.; Hillebrecht, H. Synthesis, Single-Crystal Structure and Characterization of $(CH_3NH_3)_2Pb(SCN)_2I_2$. *Angew. Chem. Int. Ed.* **2015**, *54*, 11016-11017.

(14) Yamamoto, T.; Oswald, I. W. H.; Savory, C. N.; Ohmi, T.; Koegel, A. A.; Scanlon, D. O.; Kageyama, H.; Neilson, J. R. Structure and Optical Properties of Layered Perovskite $(MA)_2PbI_{2-x}Br_x(SCN)_2$ ($0 \leqslant x < 1.6$). *Inorg. Chem.* **2020**, *59*, 17379-17384.

(15) Mączka, M.; Ptak, M.; Gągor, A.; Stefańska, D.; Sieradzki, A. Layered Lead Iodide of [Methylhydrazinium]2PbI4 with a Reduced Band Gap: Thermochromic Luminescence and Switchable Dielectric Properties Triggered by Structural Phase Transitions. *Chem. Mater.* **2019**, *31*, 8563-8575.

(16) Ma˛czka, M. a.; Ptak, M.; Ga˛gor, A.; Stefańska, D.; Zaręba, J. K.; Sieradzki, A. Methylhydrazinium Lead Bromide: Noncentrosymmetric Three-Dimensional Perovskite with Exceptionally Large Framework Distortion and Green Photoluminescence. *Chem. Mater.* **2020**, *32*, 1667-1673.

(17) Nazarenko, O.; Kotyrba, M. R.; Wörle, M.; Cuervo-Reyes, E.; Yakunin, S.; Kovalenko, M. V. Luminescent and Photoconductive Layered Lead Halide Perovskite Compounds Comprising Mixtures of Cesium and Guanidinium Cations. *Inorg. Chem.* **2017**, *56*, 11552-11564.

(18) Soe, C. M. M.; Stoumpos, C. C.; Kepenekian, M.; Traoré, B.; Tsai, H.; Nie, W.; Wang, B.; Katan, C.; Seshadri, R.; Mohite, A. D.; Even, J.; Marks, T. J.; Kanatzidis, M. G. New Type of 2D Perovskites with Alternating Cations in the Interlayer Space, $(C(NH_2)_3)(CH_3NH_3)_nPb_nI_{3n+1}$: Structure, Properties, and Photovoltaic Performance. *J. Am. Chem. Soc.* **2017**, *139*, 16297-16309.

(19) Nazarenko, O.; Kotyrba, M. R.; Yakunin, S.; Wörle, M.; Benin, B. M.; Rainò, G.; Krumeich, F.; Kepenekian, M.; Even, J.; Katan, C.; Kovalenko, M. V. Guanidinium and Mixed Cesium–Guanidinium Tin(II) Bromides: Effects of Quantum Confinement and Out-of-Plane Octahedral Tilting. *Chem. Mater.* **2019**, *31*, 2121-2129.

(20) Katan, C.; Mercier, N.; Even, J. Quantum and Dielectric Confinement Effects in Lower-Dimensional Hybrid Perovskite Semiconductors. *Chem. Rev.* **2019**, *119*, 3140-3192.

(21) DeCrescent, R. A.; Venkatesan, N. R.; Dahlman, C. J.; Kennard, R. M.; Chabinyc, M. L.; Schuller, J. A. Optical Constants and Effective-Medium Origins of Large Optical Anisotropies in Layered Hybrid Organic/Inorganic Perovskites. *ACS Nano* **2019**, *13*, 10745-10753.

(22) Shi, Z.; Ni, Z.; Huang, J. Direct Observation of Fast Carriers Transport along Out-of-Plane Direction in a Dion–Jacobson Layered Perovskite. *ACS Energy Lett.* **2022**, 984-987.

(23) Stoumpos, C. C.; Mao, L.; Malliakas, C. D.; Kanatzidis, M. G. Structure–Band Gap Relationships in Hexagonal Polytypes and Low-Dimensional Structures of Hybrid Tin Iodide Perovskites. *Inorg. Chem.* **2017**, *56*, 56-73.

(24) Daub, M.; Hillebrecht, H. From 1D to 3D: Perovskites within the System $HSC(NH_2)_2I/CH_3NH_3I/PbI_2$ with Maintenance of the Cubic Closest Packing. *Inorg. Chem.* **2021**, *60*, 3082-3093.

(25) Hempel, H.; Savenjie, T. J.; Stolterfoht, M.; Neu, J.; Failla, M.; Paingad, V. C.; Kužel, P.; Heilweil, E. J.; Spies, J. A.; Schleuning, M.; Zhao, J.; Friedrich, D.; Schwarzburg, K.; Siebbeles, L. D. A.; Dörflinger, P.; Dyakonov, V.; Katoh, R.; Hong, M. J.; Labram, J. G.; Monti, M.; Butler-Caddle, E.; Lloyd-Hughes, J.; Taheri, M. M.; Baxter, J. B.; Magnanelli, T. J.; Luo, S.; Cardon, J. M.; Ardo, S.; Unold, T. Predicting Solar Cell Performance from Terahertz and Microwave Spectroscopy. *Adv. Energy. Mater* **2022**, *12*, 2102776.

(26) Miyata, A.; Mitioglu, A.; Plochocka, P.; Portugall, O.; Wang, J. T.-W.; Stranks, S. D.; Snaith, H. J.; Nicholas, R. J. Direct measurement of the exciton binding energy and effective masses for charge carriers in organic–inorganic tri-halide perovskites. *Nat. Phys.* **2015**, *11*, 582-587.

(27) Oosterhout, S. D.; Ferguson, A. J.; Larson, B. W.; Olson, D. C.; Kopidakis, N. Modeling the Free Carrier Recombination Kinetics in PTB7:PCBM Organic Photovoltaics. *J. Phys. Chem. C* **2016**, *120*, 24597-24604.

(28) Venkatesan, N. R.; Labram, J. G.; Chabinyc, M. L. Charge-Carrier Dynamics and Crystalline Texture of Layered Ruddlesden–Popper Hybrid Lead Iodide Perovskite Thin Films. *ACS Energy Lett.* **2018**, *3*, 380-386.

(29) Chattopadhyay, S.; Kokenyesi, R. S.; Hong, M. J.; Watts, C. L.; Labram, J. G. Resolving in-plane and out-of-plane mobility using time resolved microwave conductivity. *J. Mater. Chem. C* **2020**, *8*, 10761-10766.

TOC graphic

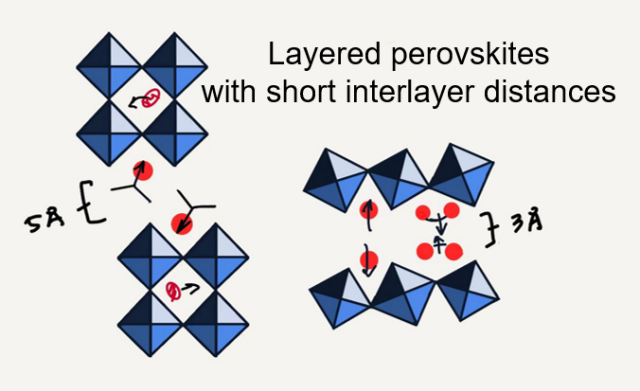

Supporting information for

Layered Hybrid Lead Iodide Perovskites with Short Interlayer Distances

Lingling Mao[1], Emily E. Morgan[2], Alice Li[2], Rhiannon M. Kennard[2], Min Ji Hong[3], Yang Liu[1], Clayton J. Dahlman[2], John G. Labram[3,4], Michael L. Chabinyc[2] and Ram Seshadri[2]*

[1]Department of Chemistry, Southern University of Science and Technology, Shenzhen, Guangdong 518055, China
[2]Materials Research Laboratory and Materials Department, University of California, Santa Barbara, California 93106, United States
[3]School of Electrical Engineering and Computer Science, Oregon State University, Corvallis, OR 97331, United States
[4]Department of Electronic & Electrical Engineering, University College London, London WC1E 7JE, United Kingdom

*Email addresses: maoll@sustech.edu.cn and seshadri@mrl.ucsb.edu

Table of contents

Section S1. Experimental details.

Materials. Iso-propylamine (99.5%), acetamidine hydrochloride (95%), lead oxide (99.9%) were purchased from Sigma-Aldrich. Hydriodic acid (55 wt % in H_2O, stabilized) and hypophosphorous acid (50 wt % in H_2O) were purchased from Spectrum Chemical. Methylammonium iodide (>99.5%) was purchased from Luminescence Technology Corp. All chemicals were used as received.

***Synthesis. (*$(IPA)_2(MA)Pb_2I_7$.** 2 mmol of PbO was dissolved in 4 ml HI and 0.5 ml H_3PO_2, 1 mmol of methylammonium iodide was added directly to the previous mixture under heating and stirring until boiling. Finally, 2 mmol of iso-propylamine was added and left to stir until clear. The solution was taken off the hotplate after the solution became homogenous. Red plate-like crystals were formed under slow-cooling to room-temperature. **$(ACA)(MA)PbI_4$.** 2 mmol of PbO was dissolved in 4 ml HI and 0.5 ml H_3PO_2, 5 mmol of methylammonium iodide was added directly to the previous mixture under heating and stirring until boiling. 3 mmol of acetamidine hydrochloride was added in the end. The solution was taken off the hotplate after becoming clear and homogenous. Red plate-like crystals were formed under slow-cooling to room-temperature. Note that for $(ACA)(MA)PbI_4$, more methylammonium iodide was needed than in the stoichiometry to prevent formation of the yellow phase $(ACA)PbI_3$. $(BA)_2PbI_4$ and $(BA)_2(MA)Pb_2I_7$ were synthesized according to literature.[1]

Single Crystal X-ray Diffraction. Full sphere data were collected using a Bruker KAPPA APEX II diffractometer equipped with an APEX II CCD detector using a TRIUMPH monochromator with a Mo Kα source (λ = 0.71073 Å) with MX Optics. Data were collected at room temperature. The collected data were integrated and a multi-scan absorption correction was applied using the APEX2 software. Crystal structures were solved by direct methods (Full-matrix least-squares on F^2) using OLEX2 program.[2]

Optical Absorption Spectroscopy. Optical diffuse reflectance measurements were performed using a Cary 5000 UV–vis–NIR spectrometer operating in the 300–8000 nm region using $BaSO_4$ as the reference of 100% reflectance. The band gap of the material was estimated by converting reflectance to absorption according to the Kubelka–Munk equation: $\alpha/S = (1 - R)^2 (2R)^{-1}$, where R is the reflectance and α and S are the absorption and scattering coefficients, respectively.

Steady-State Photoluminescence. Steady-state PL spectra were collected using HORIBA LabRAM HR Evolution Confocal RAMAN microscope. A 532 nm laser was used to excite all samples at 10× magnification.

Computational Details. Density functional theory (DFT) calculations were performed using the Vienna Ab initio Simulation Package[3-5] (VASP), version 5.4.4. The Perdew-Burke-Ernzerhof[6] (PBE) functional and projector-augmented wave[7,8] (PAW) pseudopotentials were used with a plane-wave cutoff energy of 500 eV and energy convergence of 10^{-5} eV or better. PAW potentials were chosen following the version 5.2 guidelines. Automatic k-mesh generation[9] was used with a length parameter (R_k) of 60 or better. For band-structure calculations, an appropriate **k**-path was generated using SeeK-path,[10,11] and band-structures were plotted and analyzed using Sumo.[12] For both compounds, structural relaxations were

performed in which the atomic positions, unit cell shape, and unit cell volume were allowed to relax. Van der Waals corrections were incorporated using the DFT-D2 method of Grimme.[13]

Thin-film fabrication procedure.

Materials Lead iodide (PbI_2, 99.999 %), acetamidinium iodide (ACAI, ≥ 98 %), N-N-dimethylformamide (DMF, 99.8%, anhydrous), poly (methyl methacrylate) (PMMA, MW 350000), and hydrobromic acid (HBr, ACS reagent, 48%) were purchased from Sigma Aldrich and used as received. Methylammonium iodide (CH_3NH_3I, ≥99% purity) and butylammonium iodide (≥99% purity) were purchased from Greatcell Solar. Polished z-cut quartz substrates (15 × 15 × 0.5 mm) were purchased from University Wafer.

Fabrication of thin films Quartz substrates were cleaned via ultrasonication in isopropyl alcohol for 10 min and exposed to oxygen plasma at ≈ 300 mTorr for 10 min. All subsequent solution preparation and film fabrications were performed in a nitrogen-filled glove box. Precursor solutions for (ACA,MA)PbI_4 and $(BA)_2PbI_4$ were fabricated by dissolving the precursors in stoichiometric ratios to make 0.5M solutions in DMF, and left stirring overnight at 60°C to ensure good dissolution. Films were spin-cast by dropping 40 µL of precursor solution on freshly-cleaned quartz and spin-coating at 4000 rpm for 60 seconds without antisolvent rinse, and promptly annealed at 100°C (verified by thermocouple) on a hot plate with a heat diffuser. After the films cooled, 60 µL of a PMMA solution (75 mg PMMA/3mL toluene) was spin-cast on top of the films at 2000 rpm for 30 seconds. The films were stored in a nitrogen glove box until characterization. Methylammonium lead iodide ($MAPbI_3$) control samples were fabricated mixing lead iodide (PbI2), methylammonium iodide (CH_3NH_3I), and dimethyl sulfoxide (DMSO) in a 1:1:1 molar ratio then dissolving in dimethylformamide (DMF). Films were spin-cast under atmospheric-pressure onto quartz substrates and ether was dripped a few seconds before the spin-casting ends. The $MAPbI_3$ films were then annealed as the (ACA)(MA)PbI_4 and $(BA)_2PbI_4$ films.

Film Characterizations **Powder X-Ray Diffraction** patterns were obtained using a Panalytical Empyrean powder diffractometer in reflection mode with a Cu-Kα source, operating with an accelerating voltage of 45 kV and beam current of 40 mA. **Absorbance** spectra were extracted from transmission measurements made on a Shimadzu UV-2600 ultraviolet-visible spectrophotometer at room temperature and in ambient conditions. **Photoluminescence** spectra were acquired using a Horiba FluoroMax 4 spectrometer calibrated with Milli-Q water. Photoluminescence spectra reported in in the main text were all collected using an angle of 75° between the excitation and emission port to reduce scattering. All measurements were performed with an excitation wavelength of 485 nm and a 495 nm long-pass filter was placed in front of the mission port to reduce scattering.

Time-resolved microwave conductivity (TRMC). The TRMC system used in this study is as described in a previous report[14] but a brief description is provided here for completeness. Microwaves are generated using a Sivers IMA VO4280X/00 voltage-controlled oscillator (VCO). The signal has an approximate power of 16dBm and a tunable frequency between 8GHz and 15GHz. The VCO is powered with an NNS1512 TDK-Lambda constant 12V power supply, and the output frequency is controlled by a Stahl Electronics BSA-Series voltage source. The sample is mounted inside the cavity at a maximum of the electric-field component of the standing microwaves, using a 3D-printed PLA sample holder. Microwaves reflected from the cavity are then incident on a zero bias Schottky diode detector (Fairview Microwave SMD0218). The detected voltage signal is amplified by a Femto HAS-X-1-40 high-speed amplifier (gain = ×100). The amplified detector voltage is measured as a function of time by a Textronix TDS 3032C digital oscilloscope. A Continuum Minilite II pulsed neodymium-doped yttrium aluminium garnet (Nd-YAG) laser is used to illuminate the sample. The laser pulse has a wavelength of 532 nm, a full width at half-maxima of approximately 5 ns and a maximum fluence incident on the sample of ~10^{15} photons/cm^2/pulse. An external trigger link is employed to trigger the oscilloscope before the laser fires. The photoconductance and TRMC figure of merit $\phi\Sigma\mu$ were evaluated from changes in the detector voltage using standard analysis.[15] $\phi\Sigma\mu$ was measured as a function of fluence and fitted to a model[16] that accounts for biomolecular and Auger recombination in order to evaluate representative value for sample each condition. All measurements were conducted in air, without encapsulation, in the over-coupled regime.

Table S1. Crystal data and structure refinement for $(IPA)_2(MA)Pb_2I_7$ at 298 K.

Empirical formula	$C_7H_{26}N_3Pb_2I_7$
Formula weight	1454.99
Temperature	298.0 K
Wavelength	0.71073 Å
Crystal system	Tetragonal
Space group	$P4_2/mnm$
Unit cell dimensions	a = 8.980(5) Å, α = 90° b = 8.980(5) Å, β = 90° c = 35.288(18) Å, γ = 90°
Volume	2845(3) $Å^3$
Z	4
Density (calculated)	3.396 g/cm^3
Absorption coefficient	19.409 mm^{-1}
F(000)	2496
Crystal size	0.061 x 0.058 x 0.041 mm^3
θ range for data collection	2.309 to 25.325°
Index ranges	-10<=h<=10, -9<=k<=10, -42<=l<=41
Reflections collected	12489
Independent reflections	1449 [R_{int} = 0.0878]
Completeness to θ = 25.242°	99.8%
Refinement method	Full-matrix least-squares on F^2
Data / restraints / parameters	1449 / 3 / 42
Goodness-of-fit	1.077
Final R indices [I > 2σ(I)]	R_{obs} = 0.1185, wR_{obs} = 0.2875
R indices [all data]	R_{all} = 0.1601, wR_{all} = 0.3121
Largest diff. peak and hole	5.718 and -3.290 e·$Å^{-3}$

$R = \Sigma||F_o|-|F_c|| / \Sigma|F_o|$, $wR = \{\Sigma[w(|F_o|^2 - |F_c|^2)^2] / \Sigma[w(|F_o|^4)]\}^{1/2}$ and $w=1/[\sigma^2(Fo^2)+(0.0957P)^2+616.8710P]$ where $P=(Fo^2+2Fc^2)/3$

Table S2. Crystal data and structure refinement for (ACA)(MA)PbI_4 at 293 K.

Empirical formula	$C_3H_{13}N_3PbI_4$
Formula weight	805.95
Temperature	293 K
Wavelength	0.71073 Å
Crystal system	Orthorhombic
Space group	*Imma*
Unit cell dimensions	a = 6.4676(19) Å, α = 90.00° b = 12.428(4) Å, β = 90.00° c = 18.950(6) Å, γ = 90.00°
Volume	1523.2(8) $Å^3$
Z	4
Density (calculated)	3.515 g/cm^3
Absorption coefficient	19.150 mm^{-1}
F(000)	1384
θ range for data collection	1.96 to 30.64°
Index ranges	-9<=h<=8, -17<=k<=16, -13<=l<=27
Reflections collected	4030
Independent reflections	1311 [R_{int} = 0.0367]
Completeness to θ = 30.64°	98.9%
Refinement method	Full-matrix least-squares on F^2
Data / restraints / parameters	1311 / 4 / 30
Goodness-of-fit	1.070
Final R indices [>2σ(I)]	R_{obs} = 0.0534, wR_{obs} = 0.1415
R indices [all data]	R_{all} = 0.0640, wR_{all} = 0.1512
Largest diff. peak and hole	7.643 and -1.967 e·$Å^{-3}$

$R = \Sigma||F_o|-|F_c|| / \Sigma|F_o|$, $wR = \{\Sigma[w(|F_o|^2 - |F_c|^2)^2] / \Sigma[w(|F_o|^4)]\}^{1/2}$ and calc $w=1/[\sigma^2(Fo^2)+(0.1014P)^2+2.3743P]$ where $P=(Fo^2+2Fc^2)/3$

Section S2. Structure of other related phases and powder X-ray diffraction.

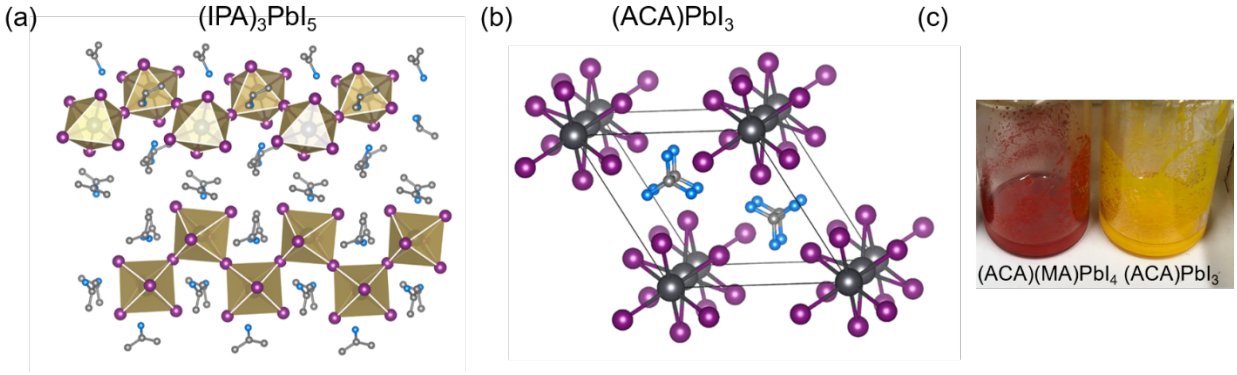

Figure S1. Crystal structure of potential secondary phases (a) $(IPA)_3PbI_5$ and (b) $(ACA)PbI_3$. (c) Sample color comparison between $(ACA)(MA)PbI_4$ and $(ACA)PbI_3$.

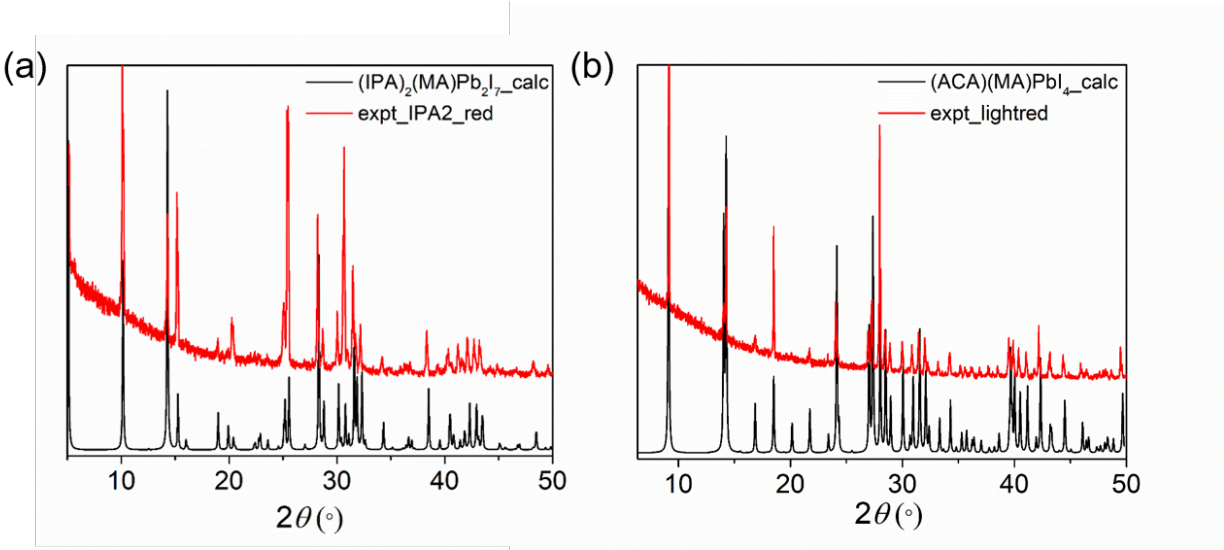

Figure S2. Experimental (red) and calculated (black) powder X-ray diffraction patterns of (a) $(IPA)_2(MA)Pb_2I_7$ and (b) $(ACA)(MA)PbI_4$.

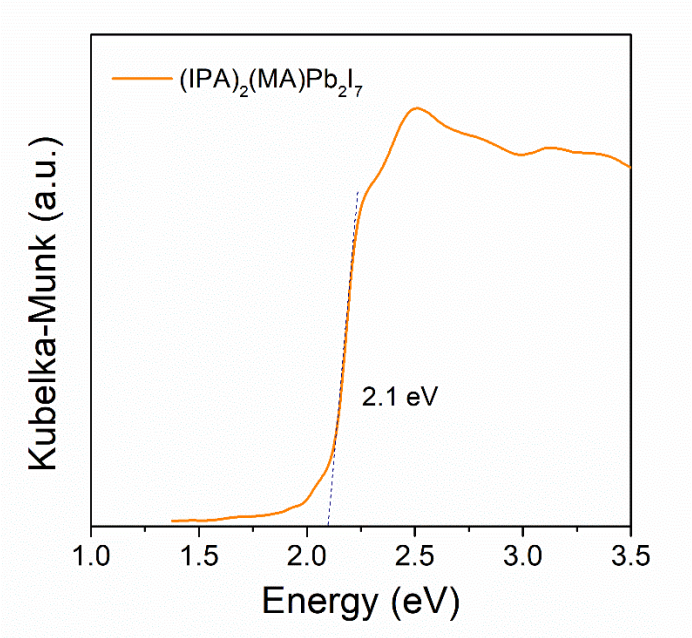

Figure S3. Re-measured absorption spectra of $(IPA)_2(MA)Pb_2I_7$ from a different batch of sample, showing the edge at ~2.10 eV.

Section S3. Additional thin-film data.

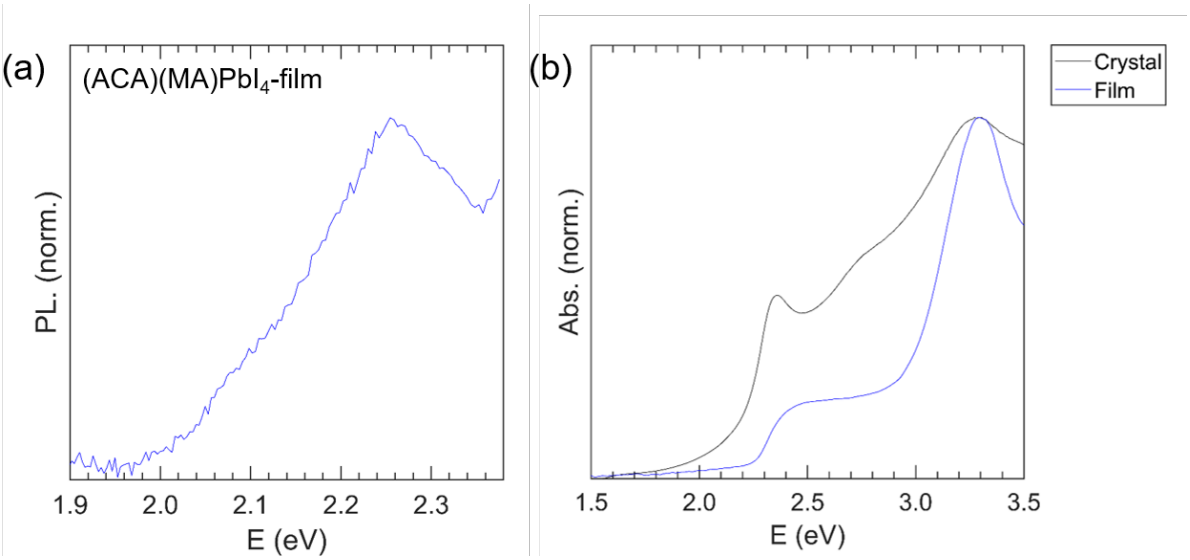

Figure S4. Room temperature steady-state PL emission spectrum and absorption spectra of $(ACA)(MA)PbI_4$ film (λ = 485 nm).

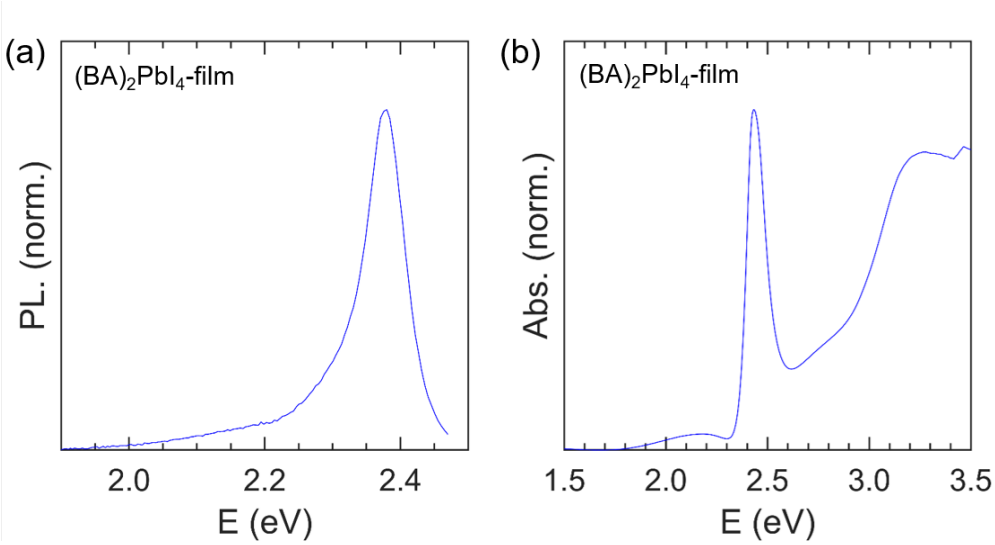

Figure S5. Room temperature steady-state PL emission spectrum and absorption spectra of $(BA)_2PbI_4$ film.

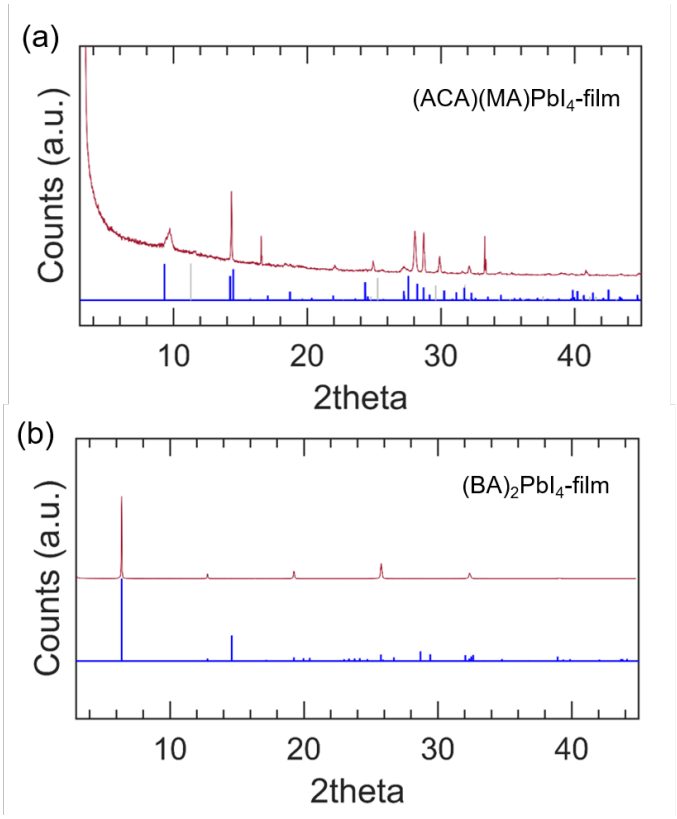

Figure S6. Experimental (red) and calculated (black) powder X-ray diffraction patterns of thin film samples of (a) $(ACA)(MA)PbI_4$ and (b) $(BA)_2PbI_4$ (show strong prefered orientation along the 001 plane, red and blue lines represent experimental and simulated peaks).

Section S4. Preliminary time-resolved microwave conductivity (TRMC) data.

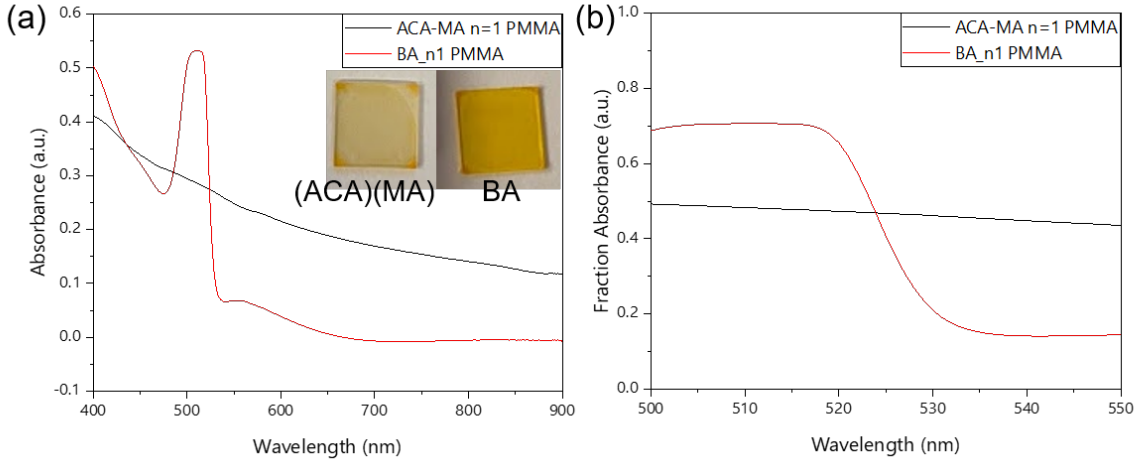

Figure S7. (a) UV-Vis optical absorption spectra of $(ACA)(MA)PbI_4$ and $(BA)_2PbI_4$ films (on quartz). (b) Fraction absorbance (at 532 nm): ACA-MA n=1 PMMA: 0.46 and BA_n=1_PMMA: 0.18.

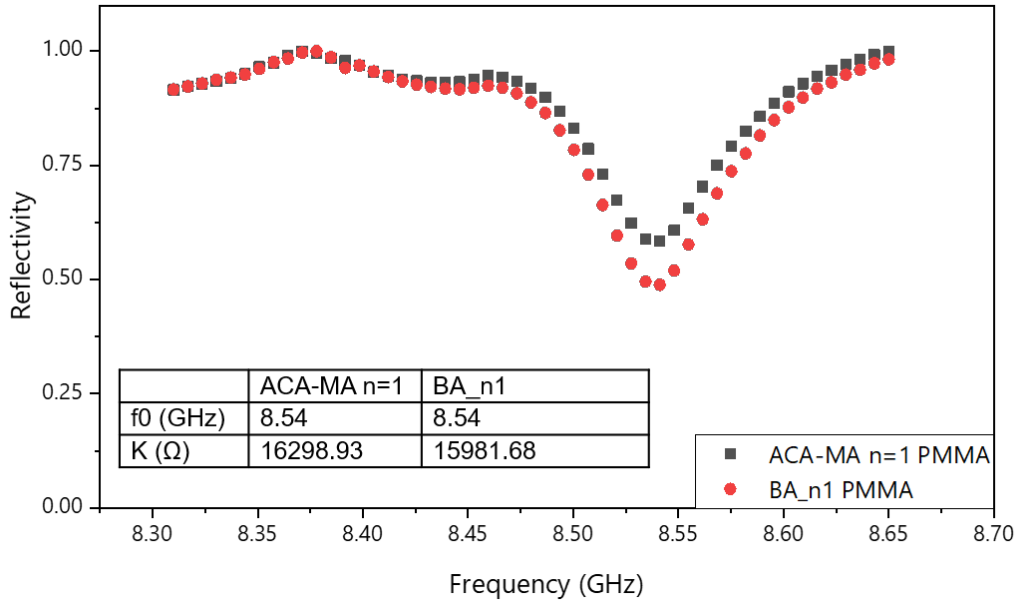

	ACA-MA n=1	BA_n1
f0 (GHz)	8.54	8.54
K (Ω)	16298.93	15981.68

Figure S8. Reflectance of microwave cavity as a function of microwave frequency when loaded with ACA-MA n=1 and BA_n=1.

Photoconductance vs. fluence:

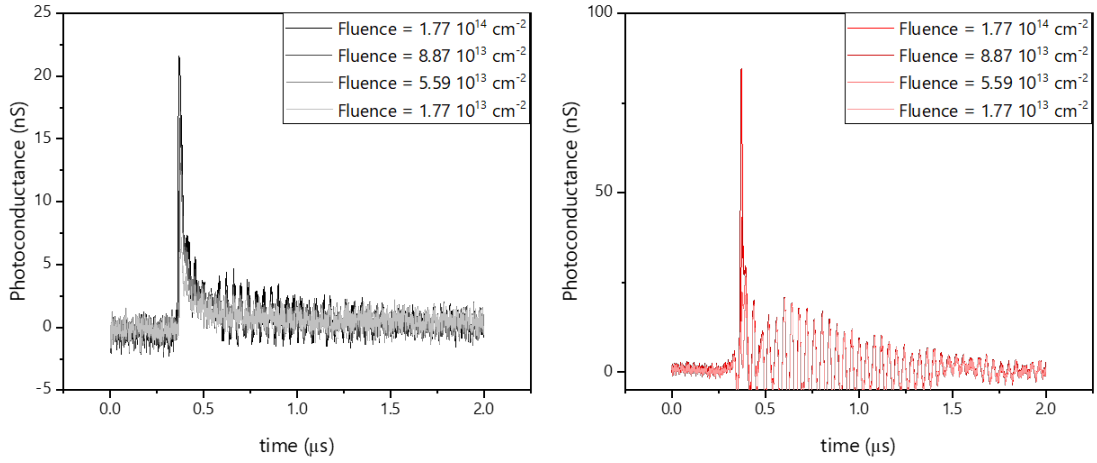

Figure S9. Photoconductance as a function of time for films of ACA-MA n=1 (black) and BA_n=1 (red) for various values of incident laser fluence, measured using TRMC.

TRMC figure of merit $\phi\Sigma\mu$:

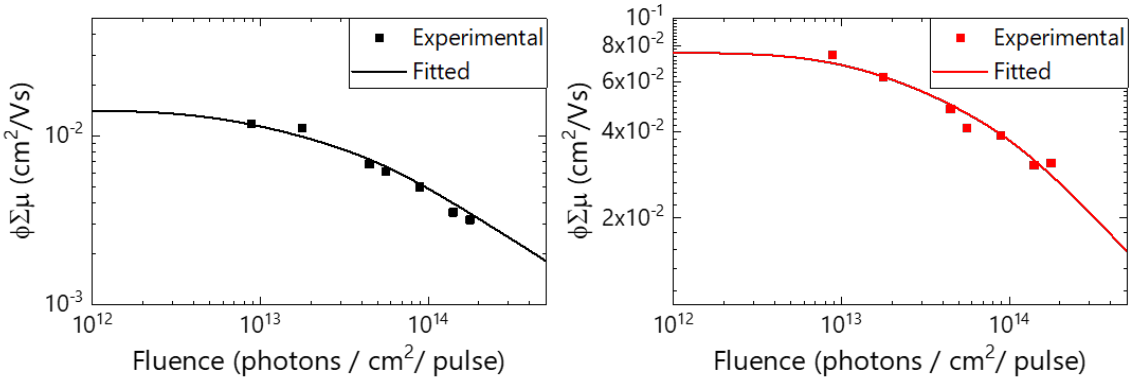

Figure S10. Points: Experimental values of the TRMC figure of merit $\phi\Sigma\mu$ (black: ACA-MA n=1, red: BA_n=1) measured as a function of incident laser fluence. Lines: fits to a model[17] which accounts for bimolecular and Auger recombination during the laser pulse, from which a representative value of $\phi\Sigma\mu$ can be extracted.

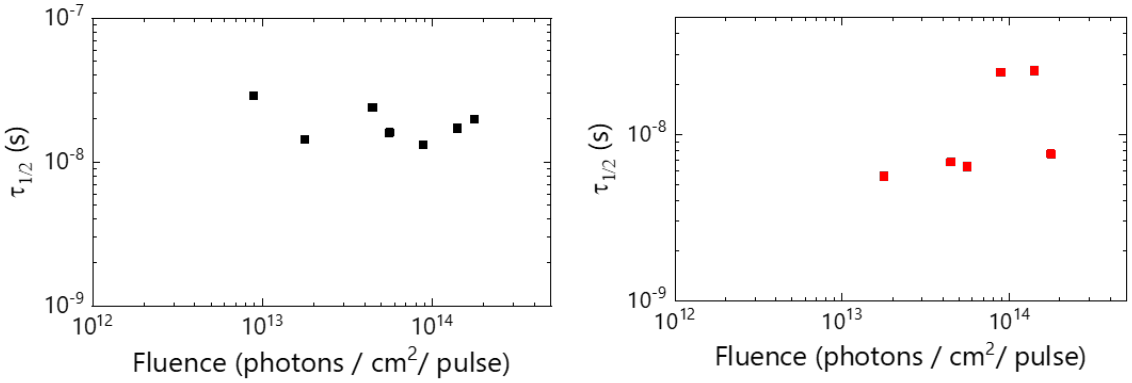

Figure S11. Approximate values of carrier half-life, $\tau_{1/2}$, measured as a function of incident laser fluence using TRMC (black: ACA-MA n=1, red: BA_n=1).

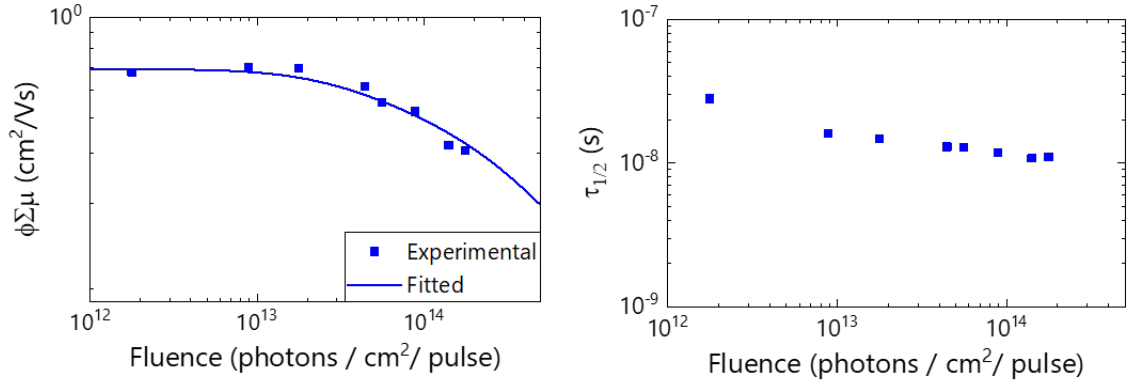

Figure S12. Left: Experimental and fitted values of the TRMC figure of merit $\phi\Sigma\mu$ as a function of fluence for control sample of 3D perovskite methylammonium lead iodide ($MAPbI_3$). Right: Approximate values of half-life, $\tau_{1/2}$, measured as a function of laser fluence for same $MAPbI_3$ control sample.

Table S3. Summary of preliminary TRMC results.

Sample	$\phi\Sigma\mu$ (cm^2/Vs)	$\tau_{1/2}$ (ns)
ACA-MA n=1 PMMA	0.014	29
BA_n=1 PMMA	0.076	5.6
$MAPbI_3$	0.66	28

References

(1) Stoumpos, C. C.; Cao, D. H.; Clark, D. J.; Young, J.; Rondinelli, J. M.; Jang, J. I.; Hupp, J. T.; Kanatzidis, M. G. Ruddlesden–Popper Hybrid Lead Iodide Perovskite 2D Homologous Semiconductors. *Chem. Mater.* **2016**, *28*, 2852-2867.

(2) Dolomanov, O. V.; Bourhis, L. J.; Gildea, R. J.; Howard, J. A.; Puschmann, H. OLEX2: a complete structure solution, refinement and analysis program. *J. Appl. Crystallogr.* **2009**, *42*, 339-341.

(3) Kresse, G.; Hafner, J. Ab initio molecular-dynamics simulation of the liquid-metal--amorphous-semiconductor transition in germanium. *Phys. Rev. B* **1994**, *49*, 14251-14269.

(4) Kresse, G.; Furthmüller, J. Efficiency of ab-initio total energy calculations for metals and semiconductors using a plane-wave basis set. *Comput. Mater. Sci.* **1996**, *6*, 15-50.

(5) Kresse, G.; Furthmüller, J. Efficient iterative schemes for ab initio total-energy calculations using a plane-wave basis set. *Phys. Rev. B* **1996**, *54*, 11169-11186.

(6) Perdew, J. P.; Burke, K.; Ernzerhof, M. Generalized Gradient Approximation Made Simple. *Phys. Rev. Lett.* **1996**, *77*, 3865-3868.

(7) Blöchl, P. E. Projector augmented-wave method. *Phys. Rev. B* **1994**, *50*, 17953-17979.

(8) Kresse, G.; Joubert, D. From ultrasoft pseudopotentials to the projector augmented-wave method. *Phys. Rev. B* **1999**, *59*, 1758-1775.

(9) Monkhorst, H. J.; Pack, J. D. Special points for Brillouin-zone integrations. *Phys. Rev. B* **1976**, *13*, 5188-5192.

(10) Hinuma, Y.; Pizzi, G.; Kumagai, Y.; Oba, F.; Tanaka, I. Band structure diagram paths based on crystallography. *Comput. Mater. Sci.* **2017**, *128*, 140-184.

(11) Togo, A.; Tanaka, I. Spglib: A Software Library for Crystal Symmetry Search. arXiv:1808.01590 [cond-mat] 2018.

(12) Ong, S. P.; Richards, W. D.; Jain, A.; Hautier, G.; Kocher, M.; Cholia, S.; Gunter, D.; Chevrier, V. L.; Persson, K. A.; Ceder, G. Python Materials Genomics (pymatgen): A robust, open-source python library for materials analysis. *Comput. Mater. Sci.* **2013**, *68*, 314-319.

(13) Grimme, S. Semiempirical GGA-type density functional constructed with a long-range dispersion correction. *J. Comput. Chem.* **2006**, *27*, 1787-1799.

(14) Hong, M. J.; Johnson, R. Y.; Labram, J. G. Impact of Moisture on Mobility in Methylammonium Lead Iodide and Formamidinium Lead Iodide. *J. Phys. Chem. Lett.* **2020**, *11*, 4976-4983.

(15) Savenije, T. J.; Ferguson, A. J.; Kopidakis, N.; Rumbles, G. Revealing the Dynamics of Charge Carriers in Polymer:Fullerene Blends Using Photoinduced Time-Resolved Microwave Conductivity. *J. Phys. Chem. C* **2013**, *117*, 24085-24103.

(16) Labram, J. G.; Chabinyc, M. L. Recombination at high carrier density in methylammonium lead iodide studied using time-resolved microwave conductivity. *J. Appl. Phys.* **2017**, *122*, 065501.

(17) Oosterhout, S. D.; Ferguson, A. J.; Larson, B. W.; Olson, D. C.; Kopidakis, N. Modeling the Free Carrier Recombination Kinetics in PTB7:PCBM Organic Photovoltaics. *J. Phys. Chem. C* **2016**, *120*, 24597-24604.